

Article

Experimental Study on Anti-Icing of Robust TiO₂/Polyurea Superhydrophobic Coating

Yizhi Du ¹, Lina Hu ^{1,*}, Liting Dong ^{1,†}, Shuming Du ^{2,†} and Dong Xu ²¹ Faculty of Electrical Engineering, Xinjiang University, 777 Huarui Street, Urumqi 830017, China² Beijing Key Laboratory of Power Generation System Functional Material, CHN Energy New Energy Technology Research Institute Ltd., Beijing 102209, China

* Correspondence: hulina@xju.edu.cn

† These authors contributed equally to this work.

Abstract: This study aims to solve the icing problem of wind turbine blades in low-temperature environments and to improve the power generation efficiency of wind turbines. In this study, modified TiO₂ particles (500 nm), butyl acetate solvent, polyaspartic acid ester polyurea (PAE polyurea), and Crestron N75 curing agent were mixed and sprayed on the epoxy resin board surface. Static icing test, dynamic icing test, wear resistance test, and icing adhesion strength test studies were carried out to evaluate the anti-icing performance of the coating as well as its mechanical stability. The results showed that the mechanical stability and anti-icing performance of the coating were relatively optimal when the ratio of modified TiO₂ particles to PAE polyurea was 1.5. Under this ratio, the static contact angle of the coating was 161.4°, and the rolling angle was 4.7°. The main reason for the superhydrophobic performance after 250 wear cycles was that the TiO₂ particles were encapsulated by PAE polyurea. The static contact angle of the coating was still greater than 150° after eight icing–de-icing cycles. This paper provides a simple method to prepare a robust superhydrophobic coating and promotes the application of superhydrophobic coatings in the field of passive anti-icing of wind turbine blades.

Keywords: superhydrophobic polyurea coating; modified TiO₂ particles; polyaspartic acid ester polyurea; anti-icing performance; mechanical stability



Citation: Du, Y.; Hu, L.; Dong, L.; Du, S.; Xu, D. Experimental Study on Anti-Icing of Robust TiO₂/Polyurea Superhydrophobic Coating. *Coatings* **2023**, *13*, 1162. <https://doi.org/10.3390/coatings13071162>

Academic Editor: Mariaenrica Frigione

Received: 22 May 2023

Revised: 15 June 2023

Accepted: 21 June 2023

Published: 27 June 2023



Copyright: © 2023 by the authors. Licensee MDPI, Basel, Switzerland. This article is an open access article distributed under the terms and conditions of the Creative Commons Attribution (CC BY) license (<https://creativecommons.org/licenses/by/4.0/>).

1. Introduction

As society seeks new energy technologies, the installed wind power capacity is growing rapidly. However, wind turbine blades are prone to icing in cold environments; ice degrades the power generation efficiency and lifetime [1] of turbines [2]. There are active and passive methods for wind turbine ice defense [3]. Active de-icing is effective, but it requires a considerable investment in equipment; it is energy-intensive, and it involves complex construction [4]. Passive de-icing methods include coating with electro-thermal materials [5–7], photothermal materials [8–10], and superhydrophobic materials [11–13]. Superhydrophobic coatings have a low surface energy and rough structure [14], so that ice does not easily nucleate; icing after adhesion is limited, and the ice that does accumulate falls off easily. A superhydrophobic coating is an effective means to solve the problem of anti-icing of wind turbine blades [15–17]. However, key problems associated with superhydrophobic coating are reducing contamination, reducing costs, and improving their mechanical stability.

In previous studies, researchers had often used polymers, such as PTFE [18], PVDF [19], and polypyrrole [20], to prepare hydrophobic coatings to solve the anti-icing problem of wind turbine blades. All these hydrophobic coatings had shown excellent anti-icing performance. In particular, the shear strength of PTFE coatings could be reduced by up to 80% compared to uncoated blades under –1.8 °C to –12.5 °C environment [21]. However, the disadvantages of these coatings were that they were expensive, not wear-resistant, and

not easily degradable. Therefore, in this study we used polyaspartic acid ester polyurea (PAE polyurea) instead of fluoropolymer. Polyurea is a new environmentally friendly material formed by the reaction of an isocyanate component with an amine component [22]. The molecular structure of polyurea contains a considerable number of urea groups, which are geometrical structures centered on C=O groups and have extremely strong hydrogen bonding and high intermolecular forces and have the advantages of corrosion resistance, high abrasion resistance, scratch resistance, high ductility, and low surface energy [23]. It had been studied in the field of anti-icing of roads [24], but there were few reports on the research in the field of anti-icing of wind turbine blades. The material of the wind turbine blade is glass-fiber-reinforced epoxy resin. PAE polyurea has good hardness after curing and can be firmly bonded to the substrate. In order to achieve superhydrophobic performance, it is usually necessary to add nanoparticles, and the common choices are nano-SiO₂ [25], nano-Fe₂O₃ [26], nano-Al₂O₃ [27], etc. In this paper, modified TiO₂ particles were used because TiO₂ particles have photocatalytic properties that can degrade the contaminants attached to the coating surface and restore the superhydrophobic properties of the coating [28].

How to maintain the superhydrophobic properties and improve mechanical stability is a hot research topic in academia. At this stage, there are two main approaches. One is to use multiple micro–nanostructures. For example, Bai et al. [29] used a suspended high-speed oxygen fuel thermal spraying system to prepare superhydrophobic ceramic surfaces with unique micro- and nanoscale structures. Peng et al. [30] prepared all-organic flexible multi-fluorinated superhydrophobic nanocomposite coatings that had both mechanical and chemical robustness. Yamauchi et al. [31] used loosely filled tetrapod-like zinc oxide to construct a “two-dimensional needle-like surface” and a “three-dimensional porous framework.” Wang et al. [32] designed micro-structured armor that had excellent mechanical robustness by splitting the wettability and robustness to two scales.

The other approach to improve the mechanical stability of superhydrophobic coatings is to construct self-healing surfaces. Guo et al. [33] constructed a self-healing superhydrophobic coating with epoxy resin and PDMS; the coating recovered the micro- and nano-rough structure by heating at 85 °C for 2 min. Wang et al. [34] prepared a superhydrophobic material with n-nineteenthane and polydimethylsiloxane that had a fast self-healing speed, and the hydrophobic property recovered within 20 min without external stimulation. Cao et al. [35] prepared self-healing superhydrophobic coatings using ultra-high polymer–silicone polymers and silica-based nanoparticles, and 10 μm cut damage was recovered by heating at 120 °C for 3 min. These methods improved the mechanical stability of the coatings to some extent, but the high cost and complicated preparation procedures make it difficult to promote their use on a large scale.

In order to overcome the shortcomings of existing methods, a simple superhydrophobic polyurea coating was proposed in this paper to solve the anti-icing problem of wind turbine blades. Firstly, TiO₂ nanoparticles were modified using per (heptadecyl) fluorodecyltriethoxysilane. Then, the superhydrophobic polyurea coating was prepared with PAE polyurea as a low surface energy substrate. Meanwhile, experimental studies on static icing, dynamic icing, icing adhesion strength, and an icing–de-icing cycle were conducted to analyze the anti-icing mechanism of a superhydrophobic polyurea coating and the effect of material ratio on the anti-icing performance.

2. Experimental Section

Combined with the current state of research at home and abroad, the anti-icing mechanism of superhydrophobic coatings can be expressed in three aspects. First, the superhydrophobic coating surface supercooled droplet slippage [36]; second, the superhydrophobic coating surface can delay the droplet icing process [37]; third, the low surface energy material of superhydrophobic coating can reduce the adhesion of ice to the substrate [38]. At the same time, the problem that the micro and nanostructures of superhydrophobic coatings are prone to wear is considered. Therefore, a static icing test, a dynamic icing test,

an ice adhesion strength test, an icing–de-icing test, and a wear-resistance test were carried out in this paper.

2.1. Materials

The substrate was a $100 \times 100 \times 2$ mm epoxy resin board. Anhydrous ethanol, butyl acetate, per (heptadecyl) fluorodecyltriethoxysilane, ammonia, and PAE polyurea were purchased from Shanghai Aladdin Reagent Co. (Shanghai, China). TiO_2 was purchased from Shanghai Mogo Technology Co. Crestron N75 curing agent was purchased from Crestron Investment Co. (Shanghai, China). The polyurea resin is polyaspartic acid ester polyurea, referred to as polyaspartate polyurea or PAE polyurea. PAE polyurea is a macromolecular polymer obtained by the reaction of aliphatic isocyanates with polyaspartic acid ester. The molecular structure of polyaspartic acid ester is shown in Figure 1a. The reaction mechanism of polyaspartic acid ester is shown in Figure 1b [39].

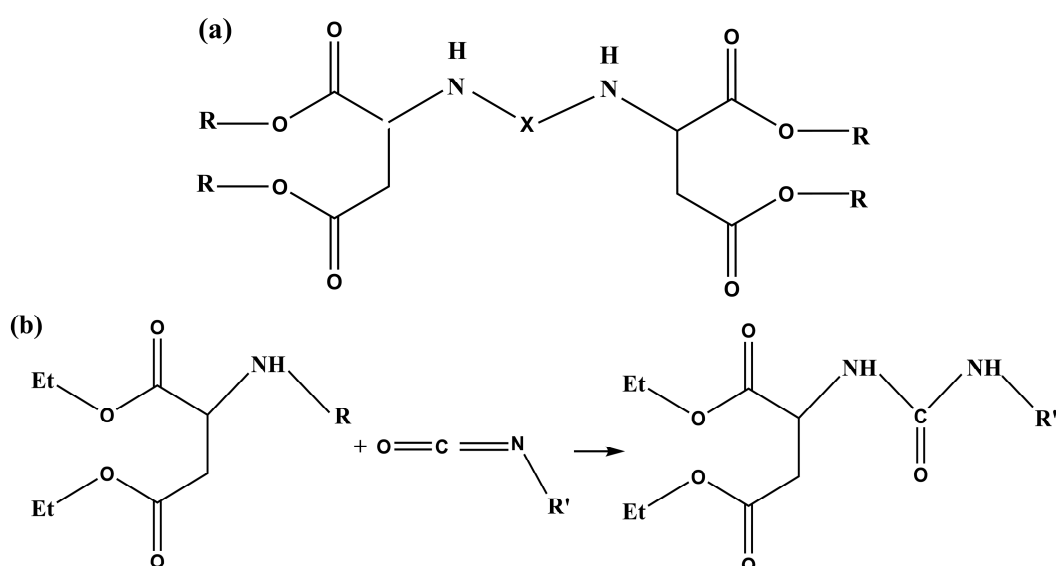


Figure 1. (a) Polyaspartic acid ester and (b) reaction mechanism of polyaspartic acid ester.

2.2. Coating Preparation

Anhydrous ethanol, TiO_2 powder with a particle size of 500 nm, and per (heptadecyl) fluorodecyltriethoxysilane (Shanghai Aladdin Reagent Co., Shanghai, China) were measured to prepare modified TiO_2 powder based on the Stober method proposed by Werner Stöber et al. [40]. The preparation process was shown in Figure 2. Firstly, 50 mL of anhydrous ethanol was measured in beaker I. A total of 10 g of TiO_2 powder with a particle size of 500 nm was added to beaker I and stirred in a magnetic stirrer at 500 rpm for 10 min. Secondly, 6 g of all (heptadecyl) fluorodecyltriethoxysilane was weighed in beaker II and stirred for 10 min. Deionized water was heated to 40°C using an electromagnetic heating stirrer. Then, the liquid from beaker I was poured into a round-bottomed flask, and the round-bottomed flask was placed in water at 40°C and heating continued. After the solution in the round-bottomed flask also reached 40°C , heating was continued for 5 min, adding 30 mL of ammonia to it and heating for 10 min. Slowly, the solution in Beaker II was added to the heating round-bottomed flask drop by drop and covered, and the reaction was continued for 2 h. Finally, the hydrophobic TiO_2 dispersion was removed and poured it into a filtering flask lined with filter paper, and a circulating water-type multi-purpose vacuum pump was connected and pumped until no water drops fell. The powder obtained from the upper layer was put into a vacuum-drying oven (Beijing Yashilin Testing Equipment Co., Beijing, China) and dried for 24 h to obtain the modified TiO_2 powder.

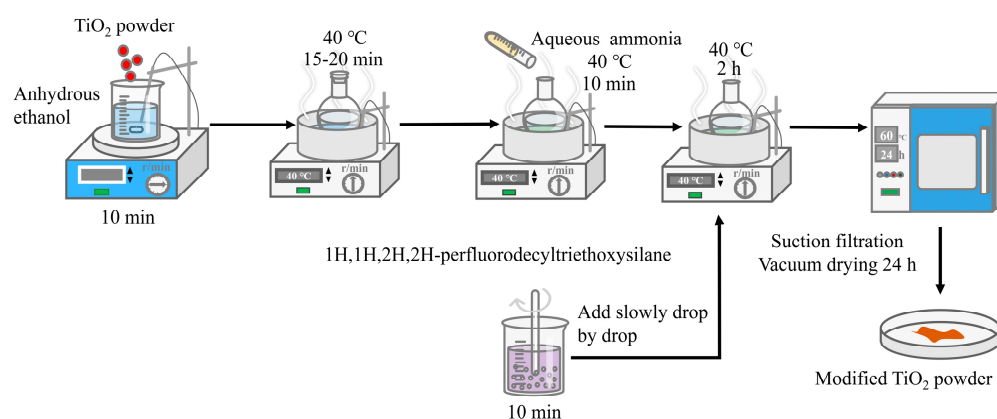


Figure 2. Preparation of modified TiO₂.

The sample substrates were a glass-fiber-reinforced epoxy resin board (Anhui Ruifa Composite Material Manufacturing Co., Anqing, China). The epoxy resin boards were sanded with 1000 grit sandpaper until there were obvious scratches. Then, the samples were cleaned with anhydrous ethanol followed by deionized water. The samples were dried after cleaning to obtain the spare substrate.

The modified TiO₂ and butyl acetate were measured in a conical flask and stirred on a magnetic mixer. Then, PAE polyurea was added dropwise to the conical flask and stirred for 10 min. Finally, Crestron N75 curing agent (Crestron Investment Co, Shanghai, China) was added; the mass ratio of PAE polyurea to Crestron N75 curing agent was 2:1, and the solution was stirred for 10 min to homogeneity. The pressure of an air compressor was set to 0.4 MPa, the solution was poured, and the sample was placed horizontally with the nozzle 20 cm away. The spray gun was moved from one end of the sample to the other end at a uniform speed, with a 10 s delay before spraying a second time. After spraying, the samples were vacuum dried for 24 h. Three types of superhydrophobic coatings with different mass ratios were prepared, i.e., samples B, C, and D. Sample A was the uncoated epoxy resin board, and samples B', C', and D' were obtained after 250 times of wear and tear of B, C, and D, respectively, as shown in Table 1. The ratios of modified TiO₂ nanoparticles to PAE polyurea were set to 1.5, 1.2, and 1, respectively. A total of 2~3 g of PAE polyurea was added while keeping the mass of modified TiO₂ at 3 g, as shown in Table 1. Butyl acetate was used as a solvent, and modified TiO₂ was used to increase the roughness of the coating. When the ratio was proportionally increased, the superhydrophobic coating performance remained the same, so Table 1 was used as an example for experimental illustration.

Table 1. Samples prepared by spray-coating method.

Samples	m (Modified TiO ₂ :Butyl Acetate Solvent:PAE Polyurea:Crestron N75 Curing Agent)
B	3 g:8 g:2 g:1 g
C	3 g:8 g:2.5 g:1.25 g
D	3 g:8 g:3 g:1.5 g

2.3. Hydrophobic Performance Test

The contact angle and rolling angle of the samples were determined with a SDC350 contact angle measuring instrument (Dongguan Sindin Precision Instrument Co., Dongguan, China). After the water drops fell onto the sample surface, the focal length of the CCD camera lens and the size of the contrasting light source were adjusted to make the water drops clearly visible. Firstly, the static contact angle and rolling angle of the water drops were measured by the static sessile drop method. The low-temperature platform angle was set to 0°, and a drop of water was dropped. The angle formed between the natural spreading of the water drop on the solid surface, and the solid surface was the

contact angle. The volume of the water drops was taken as $3 \mu\text{L}$. Each specimen was measured at five different positions for the contact angle, and the measured values were averaged. The angle of the stationary cryogenic platform was 0° , the sample was placed on the platform, and $3 \mu\text{L}$ of water droplets added. Slowly, the platform was tilted, and the angle was recorded, at which the water droplet just rolled off. The test was repeated 5 times, and the average value was taken as the rolling angle of the sample.

2.4. Static Icing Test

Considering the water vapor condensation of small droplets as well as the freezing of droplets with lower velocities indexed by the complete freezing time t_0 , the complete freezing time was defined as the time interval between the beginning of the change in the transparency of the water droplet and the creation of the ice cone tip [41,42]. The substrate temperature was $-25 \sim -5^\circ\text{C}$, the volume of water droplets was $10 \mu\text{L}$, and the freezing of the droplet was recorded in real time using a high-speed CCD camera. Five different locations were selected for each sample for testing.

2.5. Dynamic Icing Test

The water droplets hit the sample at a certain speed, and the indicator was the freezing time of the droplets, t . The experimental setup consisted of four parts: a refrigeration unit, an infusion unit, a homemade 30° tilting stand, and a computer, as shown in Figure 3. The substrate temperature was $-25 \sim -5^\circ\text{C}$. The distance between the infusion nozzle, the sample was controlled to be 10 cm, and the speed was constant, 10~15 drops per minute. The camera recorded the freezing process of the droplets and the freezing time of the droplets.

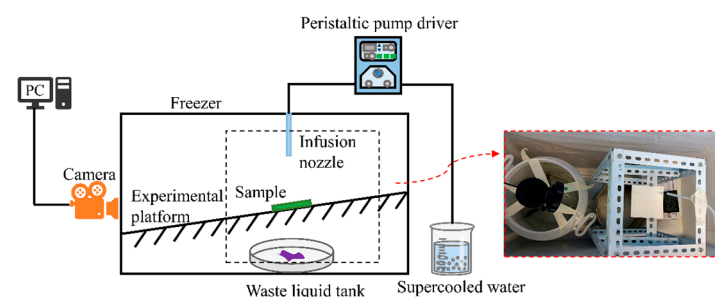


Figure 3. Dynamic icing test device.

2.6. Wear Test

A 600-mesh sandpaper sheet was fixed on the ground as the wear surface, and a 100 g weight was placed above the sample as the wear load. A thin wire was connected to the sample at one end and a linear reciprocating motor at the other end. The motor was set to run at a speed of 2 cm/s. The sample was pulled slowly with a thin wire at a uniform speed and with a force parallel to the direction of the sandpaper, so that the sample and the weight moved together. One wear event was counted from one end of the sandpaper to the other end (20 cm). After 50, 100, 150, 200, and 250 times of wear, the macroscopic shape of the sample was observed, and the contact and rolling angles were measured (see Figure 4).

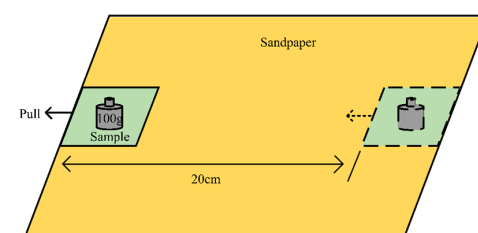


Figure 4. Wear-resistance test device.

2.7. Ice Adhesion Strength Test

Fan blade deicing mainly depends on the shear force. Therefore, the ratio of shear force to contact area was used in this paper as the ice adhesion strength of wind turbine blade surface coating. The ice adhesion strength was expressed by δ as follows:

$$\delta = F/S \quad (1)$$

where F is the shear force exerted to remove the overlying ice, and S is the contact area between the overlying ice and the object.

A $5 \times 5 \times 5$ cm box was used to prepare ice cubes on sample plates. The pull rod of the ice cover box and the tension sensor were connected, and the sample was fixed at one end and pulled slowly and uniformly at the other end to separate the measuring device from the sample surface. The value of the sensor changed to the shear force. After the samples were dried, the shear force of deicing was measured (see Figure 5). Five groups were tested at each temperature and averaged. The measured shear force was brought into Equation (1) to obtain the ice adhesion strength.

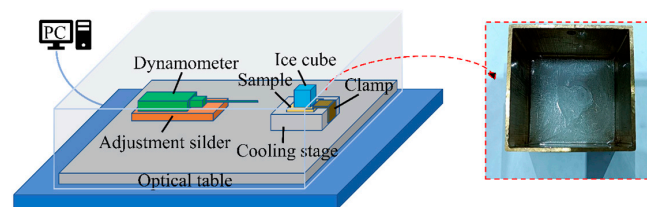


Figure 5. Ice adhesion strength test device.

3. Results and Discussion

3.1. Coating Surface Micro-Pattern Analysis

We observed the superhydrophobic surface of the samples with a Hitachi Regulus 8100 field emission scanning electron microscope (Hitachi High-Technologies (Shanghai) International Trading Co., Shanghai, China). Figure 6 shows the surface morphology of the coating. There was no significant difference in the SEM morphology of samples B, C, and D. Here, sample B was used as an example to illustrate. From Figure 6, it was found that there was a double rough structure on the surface, and the micron-level structure was the nano-TiO₂ particles and PAE polyurea that had been agglomerated, and the nano-level structure was the TiO₂ particles (485.9 nm). This structure made a large amount of air stored in the void, which could prevent the transition from Cassie state to Wenzel state to a certain extent and also had strong wear resistance, as shown in Figure 7.

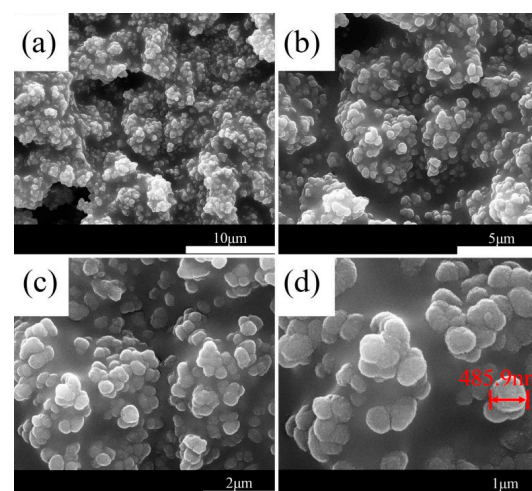


Figure 6. (a–d) SEM images of sample B surface.

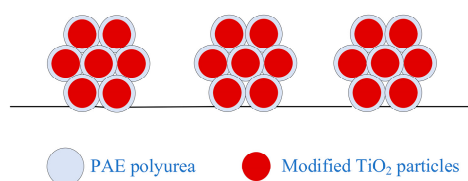


Figure 7. Double rough structure formed by PAE polyurea and modified TiO₂ particles.

3.2. Hydrophobicity Test

The contact angle and rolling angle of each sample were obtained by the test, as shown in Table 2.

Table 2. Hydrophobic properties of samples in the initial state.

Sample	Contact Angle (°)	Rolling Angle (°)
A	68.0 ± 1.34	/
B	161.4 ± 0.82	4.7 ± 0.14
C	158.7 ± 1.07	6.2 ± 0.27
D	154.5 ± 1.16	8.1 ± 0.24

The contact angles of samples B, C, and D were 154.5~161.4°, and the rolling angles were 4.7~8.1°, all of which indicated good superhydrophobic properties. As the content of the PAE polyurea increased in the sprayed solution of the samples, the magnitude of the weakening of the hydrophobic properties increased. This relation may have occurred because the sprayed solution was a homogeneous mixture of the PAE polyurea and modified TiO₂, and when the content of the PAE polyurea was lowered, the surface of the prepared coating was mostly composed of modified TiO₂, which provided sufficient rough structure and good hydrophobic properties. When the content of PAE polyurea was increased, a large amount of the PAE polyurea wrapped around the modified TiO₂, resulting in a reduction in the micro–nanostructure of the coating. The surface of the coating consisted of the micro–nanostructure of the bump and part of the PAE polyurea, resulting in the reduction in the contact angle. The larger void structure also made the water droplets less likely to roll, resulting in a larger rolling angle. The direct contact area and adhesion between the water droplets and the PAE polyurea increased, thereby further reducing the contact angle and increasing the rolling angle.

3.3. Static Icing Test

The formulations of samples A, B, C, and D preparation formulations in the figure were shown in Table 1. The complete freezing times of droplets on the surfaces of samples A, B, C, and D were 4.3 s, 16.8 s, 14.1 s, and 8.2 s at −25 °C (see Figure 8). As the temperature increased, the complete freezing times of droplets all increased accordingly, and the increased times of samples B, C, and D were larger than the freezing time of sample A. At −5 °C, the complete freezing times of samples A, B, C, and D were 10.5 s, 837 s, 756 s, and 737 s.

The complete freezing time of water droplets is an important indicator of the anti-icing performance of superhydrophobic surfaces. The longer the icing time, the more likely the droplets will be removed from the surface by external forces, such as wind and vibration. Superhydrophobic coatings have good anti-icing properties and can delay water condensation for a long time for the following reasons: When water droplets are in a non-wetting Cassie–Baxter state on a superhydrophobic surface [43–45], the rough structure traps air on the surface, and the trapped air minimizes the interaction between the droplets and the solid surface. When the surface is slightly tilted, water droplets tend to slide off [37]. In an actual freezing situation, if the water droplets fall from the surface due to gravity, the surface will not freeze. In addition, the solid–liquid–gas contact between the surface and the water droplets can efficiently reduce the heat transfer rate between the water droplets and the solid, forming a good thermal insulation layer to prevent the droplets

from freezing [46] and prolonging the freezing time of the droplets. Finally, the existence of micro- and nanostructured “space gaps” reduces the chance of uneven nucleation of ice crystals at the solid–liquid interface, decreases the adhesion of the ice layer [47], and thereby increases the freezing time of water droplets. At a temperature less than $-15\text{ }^{\circ}\text{C}$, the growth of the icing time of each sample was flat, and the growth increased abruptly when the temperature was greater than $-15\text{ }^{\circ}\text{C}$. This difference occurred because the nucleation rate and the icing process of each sample were highly affected when the temperature was low, but the advantages of the superhydrophobic coating in hindering nucleation and retarding the icing rate were highlighted when the temperature was increased [48].

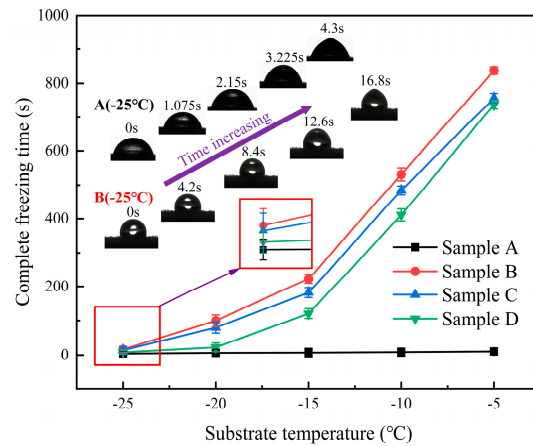


Figure 8. Complete freezing time versus temperature for a single $10\text{ }\mu\text{L}$ droplet on the surface of each sample.

3.4. Dynamic Icing Test

The dynamic freezing time of water droplets of samples A, B, C, and D all increased with the increase in substrate temperature, and the freezing times of samples B, C, and D increased significantly, compared with the flat trend of sample A. The freezing times of water droplets of samples B, C and D at different temperatures were much larger than that of sample A, and the freezing time of water droplets of sample B was slightly longer than that of samples C and D. At a substrate temperature of $-25\text{ }^{\circ}\text{C}$, the freezing times of water droplets of samples A, B, C, and D were 126.6 s, 2388 s, 1934.4 s, and 1857 s, respectively, and the freezing time of water droplets of superhydrophobic coating was on average 16.27 times as long as that of the epoxy resin board. When the substrate temperature was $-5\text{ }^{\circ}\text{C}$, the freezing times of water droplets of samples A, B, C, and D were 867.4 s, 8471.7 s, 7454.5 s, and 7524.6 s, respectively, and the freezing time of water droplets of the superhydrophobic coating was 9.01 times as long as that of epoxy resin board (see Figure 9).

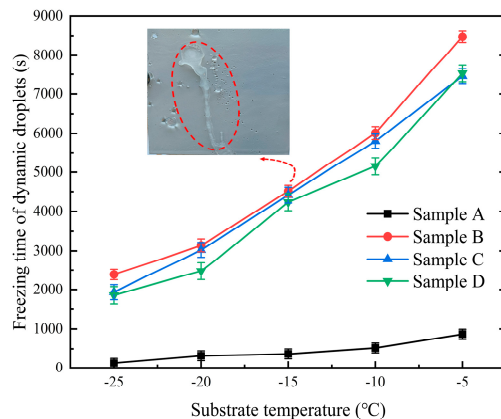


Figure 9. Effect of substrate temperature on the freezing time of dynamic droplets.

When droplets fell on the coating, the droplets tended to slide off the surface due to the compound micro–nano-level rough surface structure. The droplets immediately bounced off and split into small droplets the moment they hit the surface from a height, but these small droplets also slid away smoothly. Continuous droplet scouring accelerates the wear of the coating’s micro- and nanocomposite rough structure, thereby degrading the anti-icing performance of the surface. However, the dynamic icing performance is still advantageous compared to uncoated wind turbine blades.

3.5. Wear Test

Samples B', C', and D' in the figure were obtained from samples B, C, and D in Table 1 after 250 times of wear. As shown in Figure 10, samples B, C, and D were worn 250 times with contact angles above 150° and rolling angles within 10° , with little change compared to the initial state and remaining superhydrophobic. After 250 cycles of wear testing, the water contact angle and rolling angle were quite similar for the three coated samples.

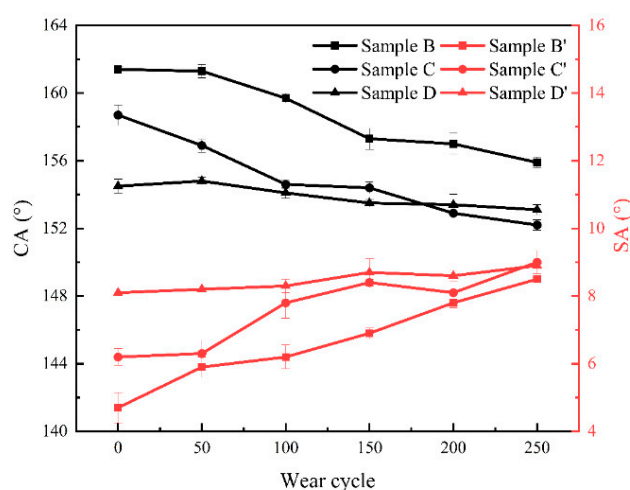


Figure 10. Effect of wear cycle on contact angle and rolling angle.

During the wear test, the coating appeared to be worn and peeled off, and the degree of wear was related to the content of PAE polyurea. Samples with more PAE polyurea content, TiO_2 particles were wrapped by PAE polyurea, and the cross-linking between PAE polyurea made the coating firmly bonded to the substrate; while samples with less PAE polyurea content could not provide a larger adhesion force and were easily destroyed. Meanwhile, the presence of modified TiO_2 particles reduced the contact area between PAE polyurea and substrate, which reduced the adhesion force between the coating and substrate. After sandpaper rubbing, the double rough structure of the sample surface was destroyed, and the bumps composed of small particles on the surface were smoothed; thus, the air layer disappeared, which, in turn, increased the contact area between the droplets and the coating, which was macroscopically reflected in the decrease in the water contact angle. Therefore, sample D had better friction resistance compared with samples A and B. With the increase in wear times, the growth of contact angle and rolling angle of sample D was lower than that of samples A and B. The coating exhibited excellent wear resistance due to the constructed double rough structure, as well as the wear resistance and low surface energy of PAE polyurea.

The superhydrophobic coating can maintain excellent performance mainly due to the constructed micro- and nanostructures, and the micro-sized PAE polyurea and nanosized modified TiO_2 in the micro- and nanostructures effectively improve the wear resistance of the coating. In addition, the modified TiO_2 and the PAE polyurea had low surface energy, which was beneficial for increasing surface roughness.

3.6. Ice Adhesion Strength

The coating surface had a micro–nanometer rough structure. The actual contact area between the ice layer and coating was smaller than the apparent contact area. Theoretically, the adhesion of the ice layer on the superhydrophobic surface should be much smaller than the adhesion of the ice layer on an ordinary material surface, which was one of the reasons why superhydrophobic coatings were anti-icing.

As shown in Figure 11, the ice adhesion strengths of ice-covered samples A, B, C, and D at $-5\text{ }^{\circ}\text{C}$ were 113.56 kPa, 54.14 kPa, 66.44 kPa, and 84.44 kPa, respectively; at $-20\text{ }^{\circ}\text{C}$, the ice adhesion strengths were 177.36 kPa, 105.92 kPa, 112.56 kPa, and 140.88 kPa. The ice adhesion strength of the superhydrophobic coating was smaller than that of the epoxy resin board. One reason for the smaller strength was because, during the icing process, the micro–nano rough structure voids of the coating were filled by air, the surface maintained the Cassie state, and the actual contact area between the coating and the ice layer was smaller [49]. Another reason was that there were many hydroxyl groups on the surface of the epoxy resin board; thus, many hydrogen bonds were formed between the epoxy resin and the ice crystals during the icing process, so the icing adhesion force on the surface of the resin was larger.

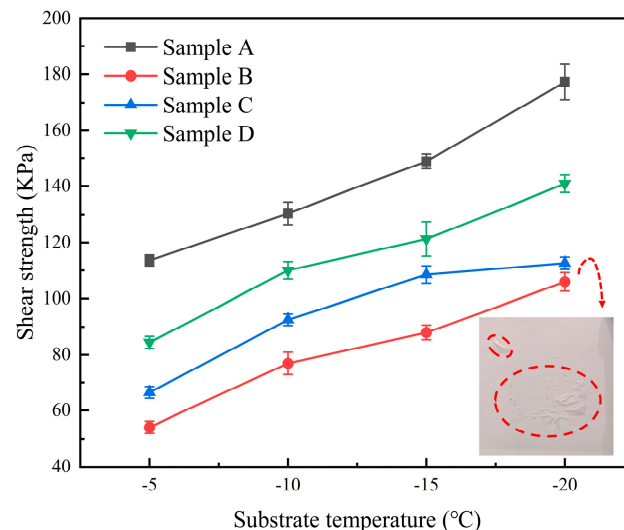


Figure 11. Effect of substrate temperature on shear strength.

As shown in Figure 12, the initial deicing strengths of samples B, C, and D at $-12\text{ }^{\circ}\text{C}$ were 50.44 kPa, 70.56 kPa, and 75 kPa, respectively, all of which were lower than 80 kPa. With the increase in the number of icing–de-icing cycles, the de-icing strengths of the samples gradually increased. After eight cycles, the shear strengths of samples B, C and D increased to 90.64 kPa, 120.28 kPa, and 128.26 kPa, which were 1.8, 1.7, and 1.71 times their initial shear strengths. The process of de-icing not only reduces part of the hydrophobic modified TiO_2 particles and destroys the low surface energy material on the particles but deicing also causes damage to the rough structure of the coating due to the pulling effect of the mechanical external force. Because of the “anchoring” effect of the ice layer in the void, the pulling damage to the rough structure is serious, resulting in the next ice repellency of the coating becoming worse when ice is applied, the ice layer is more closely combined with the coating, and the shear strength increases sharply. After eight cycles, the contact angle of the coating dropped to $146.2^{\circ}\sim 155.9^{\circ}$, and the rolling angle was $21.1^{\circ}\sim 34.0^{\circ}$, still retaining some hydrophobicity. After 250 cycles of wear, the effect of the number of cycles on the shear strength was approximately the same as before wear. Compared with the pre-wear period, the shear strength increased slightly, and the excellent wear resistance of the coating was verified.

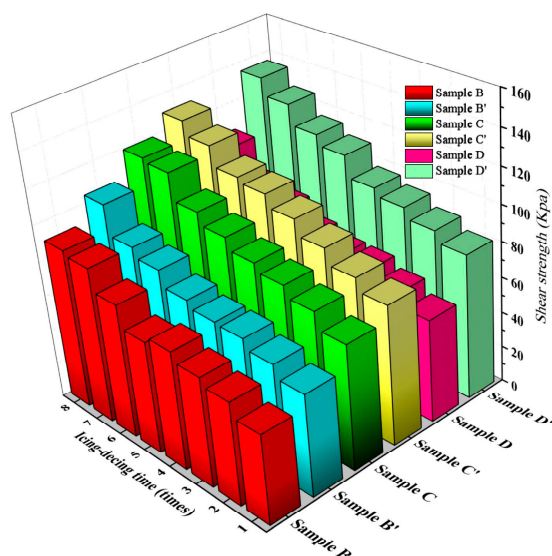


Figure 12. Effect of the number of icing–de-icing cycles on shear strength ($-12\text{ }^{\circ}\text{C}$).

4. Summary

In this paper, a robust superhydrophobic polyurea coating with good anti-icing properties was prepared. When the mass ratio of modified TiO_2 particles to PAE polyurea was 1.5, the coating exhibited the highest superhydrophobic performance and the optimal anti-icing performance. Compared with the uncoated samples, the static icing and dynamic icing times of the superhydrophobic coating were prolonged, and the icing adhesion strength was significantly reduced. This was mainly attributed to the double rough structure of the surface, which made it difficult for ice to nucleate and reduced the nucleation rate. At the same time, the presence of a large amount of air in the micro- and nanostructure reduced the contact area between the ice and the substrate. In addition, the coating had excellent mechanical stability and maintained certain hydrophobic properties after eight times of icing–de-icing tests. After 250 times of sandpaper wear tests, it still maintained superhydrophobic performance. This study provides theoretical support for the commercialization of superhydrophobic coatings applied to wind turbine blades.

Author Contributions: Conceptualization, Y.D.; methodology, L.H.; validation, L.D., S.D., and D.X.; writing—original draft preparation, Y.D. and L.H.; supervision, Y.D. All authors have read and agreed to the published version of the manuscript.

Funding: This research was funded by the Science and Technology Department of Xinjiang Uygur Autonomous Region (grant numbers: 2022B03028-4, TCBR202106, 2021D01C100).

Institutional Review Board Statement: Not applicable.

Informed Consent Statement: Not applicable.

Data Availability Statement: Not applicable.

Acknowledgments: The authors thank AiMi Academic Services (www.aimieditor.com accessed on 20 May 2023) for English language editing and review services.

Conflicts of Interest: The authors declare no conflict of interest.

References

1. El-Gohary, M. A holistic approach to the assessment of the groundwater destructive effects on stone decay in Edfu temple using AAS, SEM-EDX and XRD. *Environ. Earth Sci.* **2016**, *75*, 13. [[CrossRef](#)]
2. Jolin, N.; Bolduc, D.; Swytink-Binnema, N.; Rosso, G.; Godreau, C. Wind turbine blade ice accretion: A correlation with nacelle ice accretion. *Cold Reg. Sci. Technol.* **2019**, *157*, 235–241. [[CrossRef](#)]
3. Volpe, A.; Gaudiuso, C.; Ancona, A. Laser fabrication of anti-icing surfaces: A review. *Materials* **2020**, *13*, 5692. [[CrossRef](#)]

4. Li, W.; Zhan, Y.; Yu, S. Applications of superhydrophobic coatings in anti-icing: Theory, mechanisms, impact factors, challenges and perspectives. *Prog. Org. Coat.* **2021**, *152*, 106117. [[CrossRef](#)]
5. Chen, N.; Hu, Y.; Ji, H.; Zhang, M. Hot-air anti-icing heat transfer and surface temperature modeling. *AIAA J.* **2021**, *59*, 3657–3666. [[CrossRef](#)]
6. Liu, X.; Chen, H.; Zhao, Z.; Yan, Y.; Zhang, D. Slippery liquid-infused porous electric heating coating for anti-icing and de-icing applications. *Surf. Coat. Technol.* **2019**, *374*, 889–896. [[CrossRef](#)]
7. Zhao, Z.; Chen, H.; Liu, X.; Wang, Z.; Zhu, Y.; Zhou, Y. Novel sandwich structural electric heating coating for anti-icing/de-icing on complex surfaces. *Surf. Coat. Technol.* **2020**, *404*, 126489. [[CrossRef](#)]
8. Xue, C.H.; Li, H.G.; Guo, X.J.; Ding, Y.R.; Zhou, Y.T. Superhydrophobic anti-icing coatings with self-deicing property using melanin nanoparticles from cuttlefish juice. *Chem. Eng. J.* **2021**, *424*, 130553. [[CrossRef](#)]
9. Zhao, W.; Xiao, L.; He, X.; Cui, Z.; Fang, J.; Zhang, C.; Li, X.; Li, G.; Zhong, L.; Zhang, Y. Moth-eye-inspired texturing surfaces enabled self-cleaning aluminum to achieve photothermal anti-icing. *Opt. Laser Technol.* **2021**, *141*, 107115. [[CrossRef](#)]
10. Zhou, L.; Liu, A.; Zhou, L.; Li, Y.; Kang, J.; Tang, J.; Han, Y.; Liu, H. Facilely fabricated self-lubricated photothermal coating with long-term durability and external-replenishing property for anti-icing/deicing. *ACS Appl. Mater. Interfaces* **2022**, *14*, 8537–8548. [[CrossRef](#)]
11. Huang, X.; Tepylo, N.; Pommier-Budinger, V.; Budinger, M.; Bonaccorso, E.; Villedieu, P.; Bennani, L. A survey of icephobic coatings and their potential use in a hybrid coating/active ice protection system for aerospace applications. *Prog. Aerosp. Sci.* **2019**, *105*, 74–97. [[CrossRef](#)]
12. Lan, X.; Zhang, B.; Wang, J.; Fan, X.; Zhang, J. Hydrothermally structured superhydrophobic surface with superior anti-corrosion, anti-bacterial and anti-icing behaviors. *Colloids Surf. A Physicochem. Eng. Asp.* **2021**, *624*, 126820. [[CrossRef](#)]
13. Zhao, Y.; Yan, C.; Hou, T.; Dou, H.; Shen, H. Multifunctional $Ti_3C_2T_x$ MXene-Based Composite Coatings with Superhydrophobic Anti-Icing and Photothermal Deicing Properties. *ACS Appl. Mater. Interfaces* **2022**, *14*, 26077–26087. [[CrossRef](#)]
14. Wu, X.; Silberschmidt, V.V.; Hu, Z.-T.; Chen, Z. When superhydrophobic coatings are icephobic: Role of surface topology. *Surf. Coat. Technol.* **2019**, *358*, 207–214. [[CrossRef](#)]
15. Feng, S.; Zhu, P.; Zheng, H.; Zhan, H.; Chen, C.; Li, J.; Wang, L.; Yao, X.; Liu, Y.; Wang, Z. Three-dimensional capillary ratchet-induced liquid directional steering. *Science* **2021**, *373*, 1344–1348. [[CrossRef](#)]
16. Parent, O.; Ilinca, A. Anti-icing and de-icing techniques for wind turbines: Critical review. *Cold Reg. Sci. Technol.* **2011**, *65*, 88–96. [[CrossRef](#)]
17. Xuan, T.; Huang, J.; Liu, H.; Lou, S.; Cao, L.; Gan, W.; Liu, R.-S.; Wang, J. Super-hydrophobic cesium lead halide perovskite quantum dot-polymer composites with high stability and luminescent efficiency for wide color gamut white light-emitting diodes. *Chem. Mater.* **2019**, *31*, 1042–1047. [[CrossRef](#)]
18. Glaris, P.; Coulon, J.F.; Dorget, M.; Poncin-Epaillard, F. Thermal annealing as a new simple method for PTFE texturing. *Polymer* **2013**, *54*, 5858–5864. [[CrossRef](#)]
19. Li, K.; Hou, D.; Fu, C.; Wang, K.; Wang, J. Fabrication of PVDF nanofibrous hydrophobic composite membranes reinforced with fabric substrates via electrospinning for membrane distillation desalination. *J. Environ. Sci.* **2019**, *75*, 277–288. [[CrossRef](#)]
20. Qu, B.; Sun, Z.; Feng, F.; Li, Y.; Tong, G.; Noor, R.S. Preparation and anti-icing of hydrophobic polypyrrole coatings on wind turbine blade. *Int. J. Rotating Mach.* **2020**, *2020*, 8626457. [[CrossRef](#)]
21. Karmouch, R.; Coudé, S.; Abel, G.; Ross, G.G. Icephobic PTFE coatings for wind turbines operating in cold climate conditions. In Proceedings of the 2009 IEEE Electrical Power & Energy Conference (EPEC), Montreal, QC, Canada, 22–23 October 2009; pp. 1–6.
22. Zur, E. Polyurea—The New Generation of Lining and Coating. *Adv. Mater. Res.* **2010**, *95*, 85–86.
23. Thuy, N.T.B. Effects of additives, pigment and filler on physico-mechanical properties and weather resistance of polyurea coatings. *Vietnam J. Sci. Technol.* **2017**, *55*, 153–163. [[CrossRef](#)]
24. Chen, J.; Xie, M.; Hao, W.; Xie, P.; Wei, H. Experimental study on anti-icing and deicing performance of polyurethane concrete as road surface layer. *Constr. Build. Mater.* **2018**, *161*, 598–605. [[CrossRef](#)]
25. Seyedmehdi, S.A.; Zhang, H.; Zhu, J. Fabrication of superhydrophobic coatings based on nanoparticles and fluoropolyurethane. *J. Appl. Polym. Sci.* **2013**, *128*, 4136–4140. [[CrossRef](#)]
26. Li, Y.; Zhao, Y.; Lu, X.; Zhu, Y.; Jiang, L. Self-healing superhydrophobic polyvinylidene fluoride/ Fe_3O_4 @ polypyrrole fiber with core-sheath structures for superior microwave absorption. *Nano Res.* **2016**, *9*, 2034–2045. [[CrossRef](#)]
27. Khodaei, M.; Shadmani, S. Superhydrophobicity on aluminum through reactive-etching and TEOS/GPTMS/nano- Al_2O_3 silane-based nanocomposite coating. *Surf. Coat. Technol.* **2019**, *374*, 1078–1090. [[CrossRef](#)]
28. Aleeva, Y.; Ferrara, V.; Bonasera, A.; Martino, D.C.; Pignataro, B. Superhydrophobic TiO_2 /fluorinated polysiloxane hybrid coatings with controlled morphology for solar photocatalysis. *Colloids Surf. A Physicochem. Eng. Asp.* **2021**, *631*, 127633. [[CrossRef](#)]
29. Bai, M.; Kazi, H.; Zhang, X.; Liu, J.; Hussain, T. Robust hydrophobic surfaces from suspension HVOF thermal sprayed rare-earth oxide ceramics coatings. *Sci. Rep.* **2018**, *8*, 6973. [[CrossRef](#)]
30. Peng, C.; Chen, Z.; Tiwari, M.K. All-organic superhydrophobic coatings with mechanochemical robustness and liquid impalement resistance. *Nat. Mater.* **2018**, *17*, 355–360. [[CrossRef](#)]

31. Yamauchi, Y.; Tenjimbayashi, M.; Samitsu, S.; Naito, M. Durable and flexible superhydrophobic materials: Abrasion/scratching/slicing/droplet impacting/bending/twisting-tolerant composite with porcupinefish-like structure. *ACS Appl. Mater. Interfaces* **2019**, *11*, 32381–32389. [[CrossRef](#)]
32. Wang, D.; Sun, Q.; Hokkanen, M.J.; Zhang, C.; Lin, F.-Y.; Liu, Q.; Zhu, S.-P.; Zhou, T.; Chang, Q.; He, B. Design of robust superhydrophobic surfaces. *Nature* **2020**, *582*, 55–59. [[CrossRef](#)]
33. Guo, X.-J.; Xue, C.-H.; Sathasivam, S.; Page, K.; He, G.; Guo, J.; Promdet, P.; Heale, F.L.; Carmalt, C.J.; Parkin, I.P. Fabrication of robust superhydrophobic surfaces via aerosol-assisted CVD and thermo-triggered healing of superhydrophobicity by recovery of roughness structures. *J. Mater. Chem. A* **2019**, *7*, 17604–17612. [[CrossRef](#)]
34. Wang, Y.; Liu, Y.; Li, J.; Chen, L.; Huang, S.; Tian, X. Fast self-healing superhydrophobic surfaces enabled by biomimetic wax regeneration. *Chem. Eng. J.* **2020**, *390*, 124311. [[CrossRef](#)]
35. Cao, C.; Yi, B.; Zhang, J.; Hou, C.; Wang, Z.; Lu, G.; Huang, X.; Yao, X. Sprayable superhydrophobic coating with high processibility and rapid damage-healing nature. *Chem. Eng. J.* **2020**, *392*, 124834. [[CrossRef](#)]
36. Wang, Y.; Yao, X.; Chen, J.; He, Z.; Liu, J.; Li, Q.; Wang, J.; Jiang, L. Organogel as durable anti-icing coatings. *Sci. China Mater.* **2015**, *58*, 559–565. [[CrossRef](#)]
37. Guo, P.; Zheng, Y.; Wen, M.; Song, C.; Lin, Y.; Jiang, L. Icephobic/anti-icing properties of micro/nanostructured surfaces. *Adv. Mater.* **2012**, *24*, 2642–2648. [[CrossRef](#)]
38. Liu, T.L.; Kim, C.-J.C. Turning a surface superrepellent even to completely wetting liquids. *Science* **2014**, *346*, 1096–1100. [[CrossRef](#)]
39. Angeloff, C.; Squiller, E.P.; Best, K.E. Two-component aliphatic polyurea coatings for high productivity applications. *J. Prot. Coat. Linings* **2002**, *19*, 42–47.
40. Stöber, W.; Fink, A.; Bohn, E. Controlled growth of monodisperse silica spheres in the micron size range. *J. Colloid Interface Sci.* **1968**, *26*, 62–69. [[CrossRef](#)]
41. Vu, T.V.; Tryggvason, G.; Homma, S.; Wells, J.C. Numerical investigations of drop solidification on a cold plate in the presence of volume change. *Int. J. Multiph. Flow* **2015**, *76*, 73–85. [[CrossRef](#)]
42. Zhang, H.; Zhao, Y.; Lv, R.; Yang, C. Freezing of sessile water droplet for various contact angles. *Int. J. Therm. Sci.* **2016**, *101*, 59–67. [[CrossRef](#)]
43. Fan, P.; Pan, R.; Zhong, M. Ultrafast laser enabling hierarchical structures for versatile superhydrophobicity with enhanced Cassie–Baxter stability and durability. *Langmuir* **2019**, *35*, 16693–16711. [[CrossRef](#)]
44. Pan, R.; Cai, M.; Liu, W.; Luo, X.; Chen, C.; Zhang, H.; Zhong, M. Extremely high Cassie–Baxter state stability of superhydrophobic surfaces via precisely tunable dual-scale and triple-scale micro–nano structures. *J. Mater. Chem. A* **2019**, *7*, 18050–18062. [[CrossRef](#)]
45. Zhang, X.; Zhu, W.; He, G.; Zhang, P.; Zhang, Z.; Parkin, I.P. Flexible and mechanically robust superhydrophobic silicone surfaces with stable Cassie–Baxter state. *J. Mater. Chem. A* **2016**, *4*, 14180–14186. [[CrossRef](#)]
46. Zhang, Z.; Liu, X.-Y. Control of ice nucleation: Freezing and antifreeze strategies. *Chem. Soc. Rev.* **2018**, *47*, 7116–7139. [[CrossRef](#)]
47. Qi, C.; Lei, X.; Zhou, B.; Wang, C.; Zheng, Y. Temperature regulation of the contact angle of water droplets on the solid surfaces. *J. Chem. Phys.* **2019**, *150*, 234703. [[CrossRef](#)]
48. Huang, L.; Liu, Z.; Liu, Y.; Gou, Y.; Wang, L. Effect of contact angle on water droplet freezing process on a cold flat surface. *Exp. Therm. Fluid Sci.* **2012**, *40*, 74–80. [[CrossRef](#)]
49. Huré, M.; Olivier, P.; Garcia, J. Effect of Cassie–Baxter versus Wenzel states on ice adhesion: A fracture toughness approach. *Cold Reg. Sci. Technol.* **2022**, *194*, 103440. [[CrossRef](#)]

Disclaimer/Publisher’s Note: The statements, opinions and data contained in all publications are solely those of the individual author(s) and contributor(s) and not of MDPI and/or the editor(s). MDPI and/or the editor(s) disclaim responsibility for any injury to people or property resulting from any ideas, methods, instructions or products referred to in the content.